AIAA JOURNAL
Vol. 44, No. 3, March 2006

Numerical Study of Restricted Shock Separation in a Compressed Truncated Perfect Nozzle

Taro Shimizu* and Hiroshi Miyajima†
Japan Aerospace Exploration Agency, Ibaraki 305-8505, Japan
and
Masatoshi Kodera‡
Japan Aerospace Exploration Agency, Miyagi 981-1525, Japan

The origin of the transition of the flow structure between free shock separation and restricted shock separation in a compressed truncated perfect nozzle is studied. A three-dimensional compressible Navier–Stokes solver is used to capture the nonaxisymmetric unsteady flow structure inside the nozzle. The transition is numerically reproduced under the experimental condition where the transition occurs. Until now, the transition has been numerically observed in a thrust optimized nozzle, a parabolic nozzle, and a highly compressed truncated perfect nozzle, where an internal shock generated from the nozzle throat is the characteristic. However, in the compressed truncated perfect nozzle studied here the internal shock is weak and cannot be detected by the well-known shock function. Therefore, a function is used to detect the compression and expansion and it is found that a low-expansion region exists inside the compressed truncated perfect nozzle. The transition is likely to occur when this region is broadened radially at a mixture ratio lower than the design value.

Nomenclature

c	=	speed of sound
NPR	=	nozzle pressure ratio, p_c/p_a
O/F	=	mixture ratio; mass flow rate ratio of oxidizer (oxygen) to fuel (hydrogen)
p	=	pressure
T	=	temperature
$\boldsymbol{u}$	=	velocity

Subscripts

a	=	ambient
c	=	chamber

Introduction

ONE of the most important design factors for an effective rocket engine is optimizing the nozzle contour to obtain maximum thrust under the limits of the whole engine system. Therefore, thrust optimized (TO), parabolic, truncated perfect (TP), and compressed truncated perfect (CTP) nozzle designs are developed to increase steady performance.[1–3] However, the unsteady behavior of the flow structure inside the nozzle should be considered in the design process in addition to the steady performance of the nozzle. This is because a large side load and high thermal stress on the nozzle wall can be generated during the transient of the operation by nonaxisymmetric behavior of the separation line and reattachment of the separated flow.[4] The large side-load generation in the rocket nozzle during the startup and shutdown transients can induce serious launch problems and also might destroy engine hardware in sea-level tests. To avoid the side load, a great deal of work has been done experimentally and numerically to clarify the origin of the side-load generation.[4–21] Inside the TO, parabolic, and highly compressed truncated nozzles, an internal shock is generated by the nozzle contour. At a certain pressure ratio, this internal shock, usually originating just downstream of the throat, forms an inverse Mach reflection at the central portion farther downstream of the throat, enhancing the momentum of the flow toward the nozzle wall. Therefore, the transition of the flow structure, from free shock separation (FSS) to restricted shock separation (RSS) and vice versa, could occur and create a sudden change of the pressure distribution on the nozzle wall, generating side loads.[5,6]

In developing the LE-7A engine (initially designed as a CTP nozzle) of the Japanese H-IIA launch vehicle, we were faced with a side load originating in the transition of the flow structure during the startup and shutdown transients.[15–19]

The purpose of this study is to clarify the mechanism inducing the flow transition inside a CTP nozzle. It is also our interest to verify whether the cause of the transition inside the TO and parabolic nozzles[5,6] can explain the transition inside the CTP nozzle studied here. The numerical study concerning RSS flow has primarily used a two-dimensional axisymmetric flow simulation and assumed that an asymmetric flow is to take place during the transition.[19–21] We performed an unsteady computation in a full three-dimensional volume to obtain the real flow structure and estimated the magnitude of the side load. The results show that the transition from FSS to RSS depends on the O/F, which has been observed only in the experiment,[16,17] and that the three-dimensional flow structure of the transition is well captured. The magnitude of the calculated side load is in good agreement with the firing test. It is found that inside the CTP nozzle studied here, the internal shock that is reported to be inherent to the TO and parabolic nozzles was weak and could not be detected. However, we found that the radial width of a low-expansion region defined here plays an important role in deciding whether the transition occurs.

Numerical Method

A numerical method of solving the Navier–Stokes equations on the hybrid grid was developed using a finite volume cell vertex scheme and the lower–upper symmetric Gauss–Seidel implicit time integration algorithm (see Ref. 22). The Goldberg–Ramakrishnan model[23] was used to evaluate the turbulent kinetic viscosity, and the Venkatakrishnan limiter function[24] was used to enhance the convergence. In some unsteady calculations, Newtonian subiteration was implemented based on the Crank–Nicholson method to ensure time accuracy (see Ref. 25).

Received 28 October 2004; revision received 5 September 2005; accepted for publication 3 October 2005.

*Engineer, Tsukuba Space Center, Institute of Space Technology and Aeronautics, 2-1-1, Sengen, Tsukuba.

†Invited Researcher, Tsukuba Space Center, Institute of Space Technology and Aeronautics, 2-1-1, Sengen, Tsukuba.

‡Researcher, Kakuda Space Center, Institute of Space Technology and Aeronautics, 1, Koganezawa, Kimigaya, Kakuda.

To take the O/F effect into account, the adopted code should treat the variation of properties of the gas mixture. The code incorporates the standard finite reaction rate model for the H_2–O_2 reaction including nine species (H_2, O_2, H_2O, H, HO_2, OH, O, H_2O_2, and N_2). However, a greatly simplified frozen chemistry model with constituting species being H_2O and H_2 was used for reducing CPU time. The justification of this simplification will be described hereafter. The mass fraction and the total temperature inside the combustion chamber is calculated in the equilibrium condition under a given total pressure p_c and a mixture ratio. This is used for the inlet nozzle condition for preliminary axisymmetric simulations for a nonequilibrium chemistry, full-expansion condition. The result shows that almost all of the region downstream of the nozzle throat is occupied by H_2O and H_2 at O/F less than 8. We found that there was no major difference in the Mach isolines inside the nozzle between the nonequilibrium and the frozen calculations. Therefore, we simplify the inlet condition as follows. Only two species, H_2O and H_2, flow into the nozzle with a constant total temperature, depending on the mixture ratio and the total pressure, which is increased to simulate the startup transient. This assumption reduces the numerical cost and also makes the mutual comparison of the flow structures clear and meaningful because, for example, if O/F is the same, the Mach isolines are identical for different nozzle pressure ratio (NPR) as long as the flow continues to be expanded (until the generation of shock waves).

We briefly explain the design of the nozzle studied here. Based on the CTP design method, a TP nozzle contour is axially compressed by 5%, that is, a factor of 0.95 was multiplied to the axial coordinate of the TP contour. The discontinuity between the initial circular contour and the compressed TP contour is smoothly connected. The nominal chamber pressure and the nominal mixture ratio is 12.4 MPa and 6, respectively. The geometrical area ratio is 52. Figure 1 shows the whole computational region for the LE-7A nozzle. The intersection of the entire calculated region with a symmetry plane including the axis is presented. The distance in the axial direction from the nozzle throat to the exit is 30,000 mm, and the radius of the outer boundary of the cylinder is 6000 mm. Figure 2 shows an enlarged grid distribution including the nozzle. The grid points are concentrated near the throat and a step for film cooling port denoted by A. (See also Fig. 3.) The total cell number is approximately 12 million. The nozzle surface is divided by 240 to 480 in the circumferential direction (Fig. 4). The computational

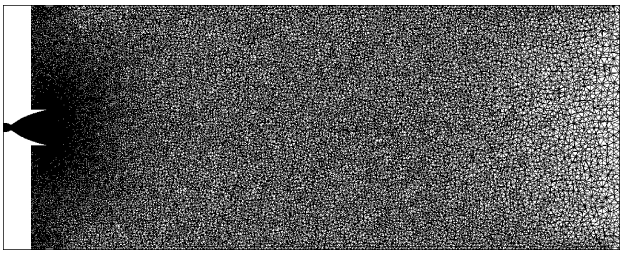

Fig. 1 Computational grid distribution on symmetric plane for LE-7A nozzle.

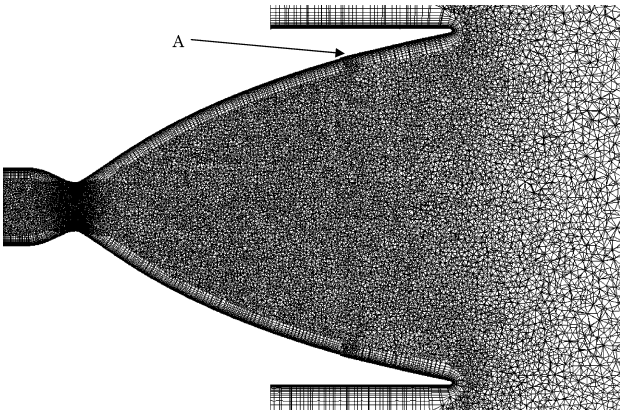

Fig. 2 Computational grid distribution on symmetric plane for LE-7A nozzle, nozzle part expanded.

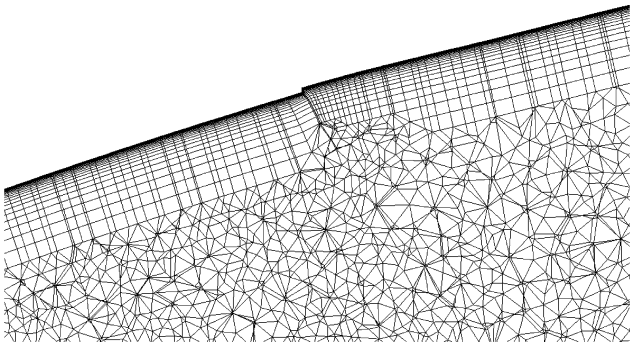

Fig. 3 Computational grid distribution near step for film cooling port.

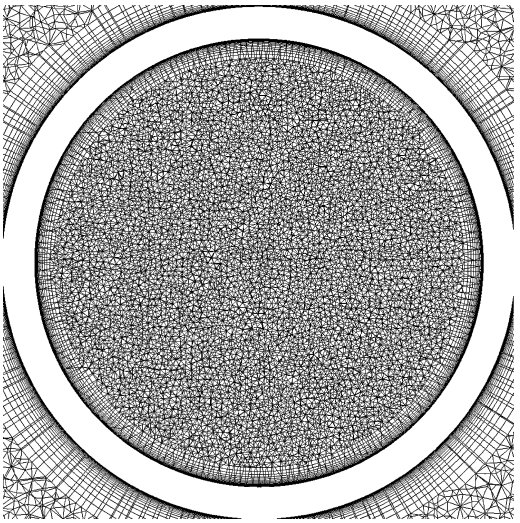

Fig. 4 Computational grid distribution on plane perpendicular to symmetry axis of nozzle, 150 mm downstream of step for film cooling port.

cost necessary to perform three-dimensional unsteady calculations is enormous. Therefore, we first conducted the numerical simulations on some grids varying the nozzle division under a typical flow condition. Because the steady flow properties such as Mach number and pressure distributions and the O/F inducing RSS flow are the same, all presented results are calculated on one of the grids tested. The calculation was performed using the Earth Simulator of the Japan Agency for Marine–Earth Science and Technology.

Computational Results

Initially, the inside of the nozzle and the surroundings are filled with standard air, $T = 300$ K and $p_a = 0.1$ MPa. A mixture of H_2O and H_2 at a constant total temperature corresponding to a specified O/F flows into the nozzle with increasing total pressures. The temperature of the nozzle wall is assumed to be 700 K throughout the calculation.

In the startup and shutdown transient, the O/F fluctuates sharply in the actual operation. Although the nominal value for the O/F designed for the steady condition is about six, the transient value can be from three to eight for a short period of time. The 1/10 subscale experiment[16,17] demonstrated the flow transition by shadowgraphs and the measurement of the side load. In the startup transient, the flow transition from FSS to RSS is likely to occur at a lower O/F, 2.8–4.1, than the designed value 6 where only FSS is observed. Therefore, in the numerical simulation, the startup transient flow structures for O/F corresponding to six and three are investigated in detail. Table 1 summarizes the gas condition of the nozzle inlet for the simulation. The transition mechanism is explained by analyzing the flow properties that are difficult to obtain by experiment alone.

General Flow Structure

Figure 5 shows the wall pressure and Mach number distribution when $O/F = 3$, showing the transition from FSS to RSS. The

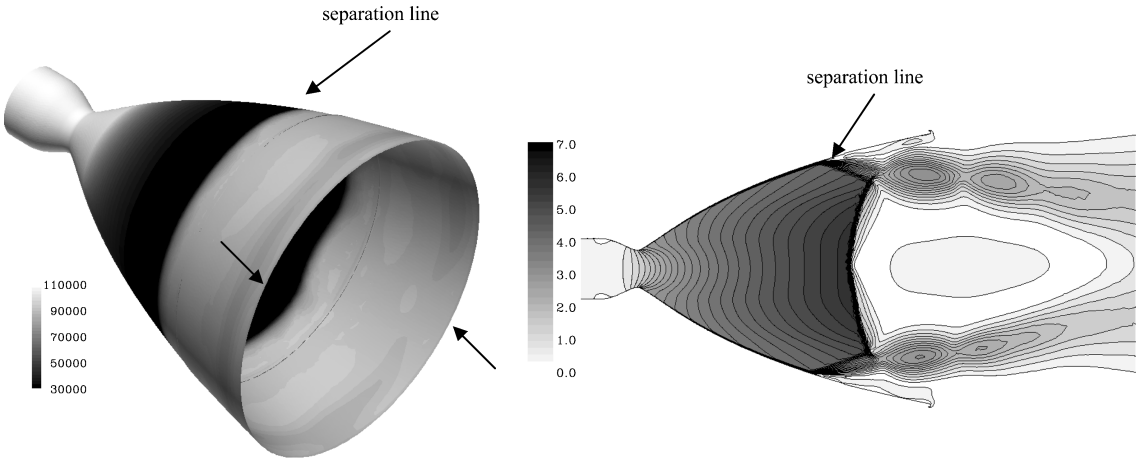

a) NPR = 49

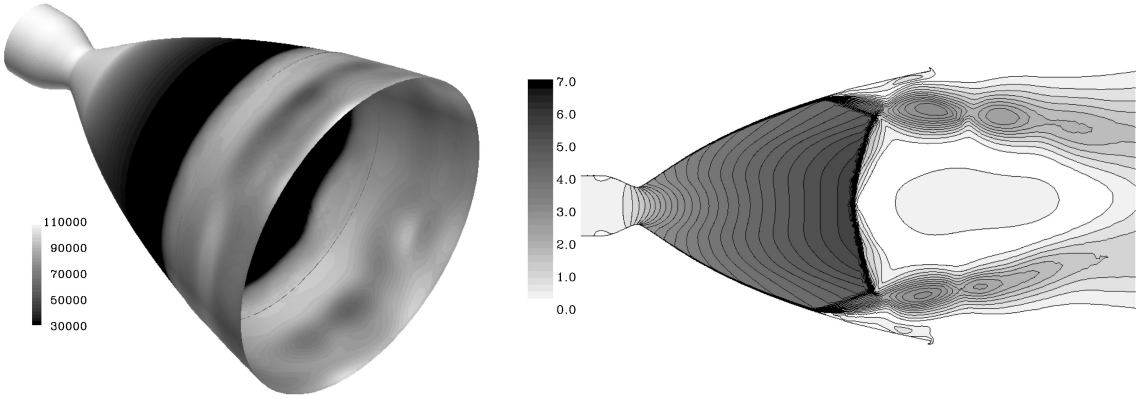

b) NPR = 50

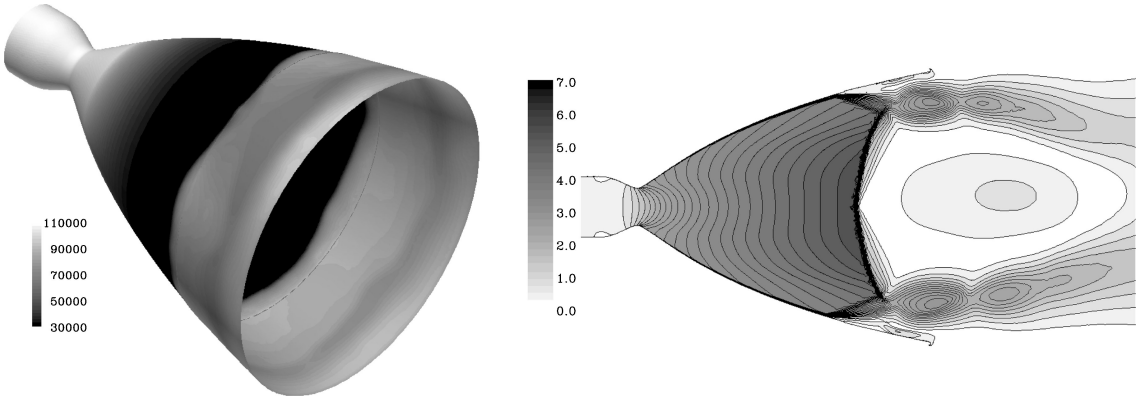

c) NPR = 51

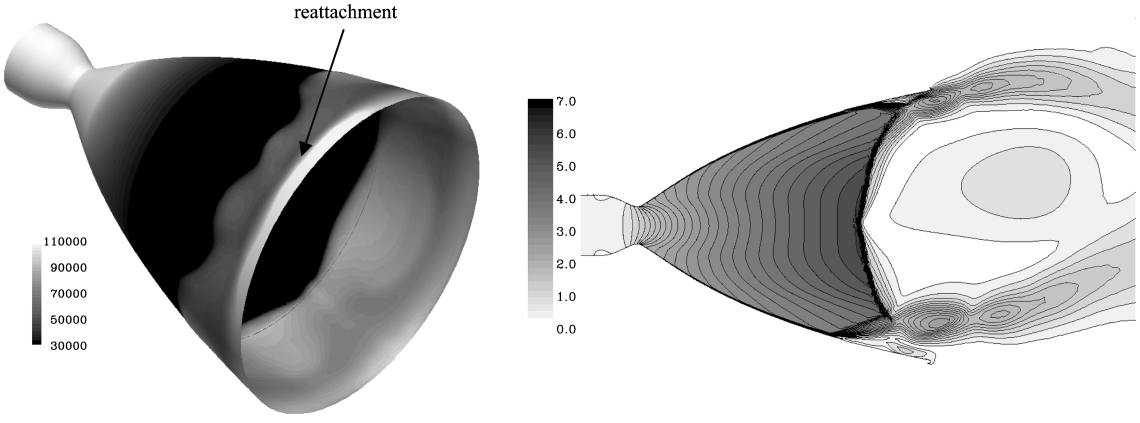

d) NPR = 52

Fig. 5 Wall pressure (pascals; left) and Mach number distribution (right), *O*/*F* = 3.

Table 1 Gas condition of the nozzle inlet

	O/F	
Condition	6	3
T_c, K	3500	2500
H_2O mass fraction	0.964	0.844
H_2 mass fraction	0.036	0.156

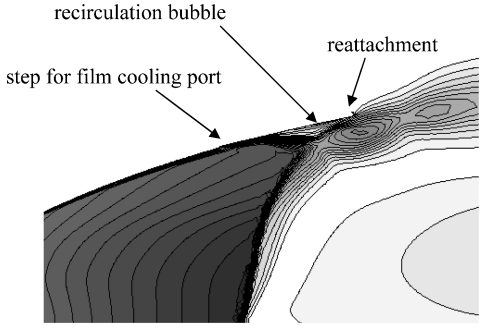

Fig. 6 Enlargement of Mach number distribution including flow reattachment in Fig. 5d.

two arrows at the nozzle exit (Fig. 5a) indicate the circumferential position of the two-dimensional Mach number distribution. The rate of the increment of the NPR per microsecond is 0.05, which is of the same order as in real operation of the LE-7A engine. When NPR = 49, the separation line is nearly symmetric. The wall pressure behind the separation line remains at nearly ambient pressure, and the flow structure is FSS. When NPR = 50, the region between the supersonic jet and the wall narrows. In this region, aspired inflow of ambient air is accelerated, resulting in decreased wall pressure (the dark part upstream of the nozzle exit in Fig. 5b). As a result, when NPR = 51, a part of the separation line moves downstream passing the step for film cooling ports. Also, a small increase of the wall pressure at the nozzle exit is observed, indicating that the supersonic jet is approaching the nozzle wall. Because the separation shock location is determined to balance the pressure gap, once the wall pressure downstream is decreased, the corresponding part of the separation line moves downstream inducing a further decrease in wall pressure. Thus, part of the deformed separation line moves downstream suddenly, generating the recirculation bubble and RSS flow structure shown in Fig. 5d. Figure 6 is the enlargement of the Mach number distribution including the flow reattachment in Fig. 5d. The wall pressure of the reattachment (the white part in Fig. 5d) at the nozzle exit is 0.15 MPa. The imbalance of the circumferential pressure distribution (the different flow structure between FSS and RSS) generates a large side load. We presume that the infinitesimal asymmetry of the flow is generated from an intrinsic asymmetry of the unstructured grid. However, once developed to a certain level such as computed here, the flow asymmetry has physical significance independent of the initial small disturbances. In a real engine operation, various geometrical and operating parameters, as well as their disturbances, decide the temporal behavior of the sudden transition between the two stable flow structures (FSS and RSS).

A comparison of the magnitude of side loads between calculated and measured is of significance. The magnitude of the calculated side load is 120 kN at NPR = 52, which is in accord with the firing test, 75–100 kN. The side loads are compared by the magnitude measured at an actuator of the engine. If the NPR is increased from 52, the reattached part passes the nozzle exit and the flow structure becomes FSS again. This is called the end effect, which is another cause of a side load. Although a slight distortion of the separation line is observed at $O/F = 6$, the supersonic jet stays away from the nozzle wall (Fig. 7). Therefore, the wall pressure behind the separation line is nearly equal to the ambient pressure, and the transition to RSS does not occur. The magnitude of the calculated side load is 20 kN at NPR = 52.

In both cases, a cap shock type pattern is observed, and the circulation region is formed downstream. However, the curvature of the cap shock is larger when $O/F = 6$ than when $O/F = 3$. The agreement between the simulation and the experiment in the NPR where the large side load occurs and the O/F at which the transition from FSS to RSS is obtained is reasonably good. NPR = 35 ~ 59 and $O/F = 2.8 \sim 4.1$ in the subscale experiment.[16] Therefore, it is shown in both computational simulation and the experiment that the O/F, in other words, the ratio of specific heat, has an important effect on the flow transition.

Capture of Fine Flow Structure

Next, the obtained flow structure inside the CTP nozzle (LE-7A original nozzle) is compared with that inside other nozzles. Inside TO and parabolic nozzles an internal shock is generated from the throat, and an inverse Mach reflection at the centerline downstream of the throat forms a cap shock structure.[6] Thus, the momentum of the flow toward the nozzle wall increases, hence, pushing the supersonic jet toward the nozzle wall, resulting in the generation of RSS flow (Fig. 8). However, little is known about a CTP nozzle. In particular, although the cap shock structure is observed independent of the O/F, it is not clear whether the bending contour of the Mach number corresponds to the internal shock wave, which is characteristic of TO and parabolic nozzles. Therefore, using the shock function,[26] we first investigate whether an internal shock exists. The shock function is defined as follows:

$$f(\boldsymbol{x}) \equiv \frac{\boldsymbol{u}}{c} \cdot \frac{\text{grad } p}{|\text{grad } p|}$$

This function represents the Mach number of the velocity component perpendicular to the pressure discontinuity. Therefore, if a shock wave exists, the function changes from greater than one upstream to less than one downstream. The contour line where $f(\boldsymbol{x}) = 1$ is satisfied indicates the shock wave. When this function is applied to numerical results, the contour usually includes several cells, depending on the resolution of the shock wave. Figures 9 and 10 show the contour where $f(\boldsymbol{x}) = 1$ is satisfied when the $O/F = 3$ and 6 under the full-flow condition, NPR = 124. The white points indicate $f(\boldsymbol{x}) = 1$. In both Figs. 9 and 10, we can observe the cap shock structure, the separation shock emanating from the nozzle lip, the small shock from the step for film cooling ports, and the shock waves included in the supersonic jet. Although there are regions where the contour of the Mach number is bent and concentrated, which suggests the concentration of compression waves, no shock wave is detected. Compression waves generated from the wall contour downstream of the initial expansion (circular arc) may coalesce into a shock wave depending on the compression ratio of the TP nozzle and the smoothing technique in connecting the circular arc and the downstream contour. We believe that for the CTP nozzle studied here, the internal shock wave, if it exists, is too weak to be detected by the shock function under the mesh size used.

It is necessary to investigate in detail the compression and expansion in the flowfields to understand the difference of flow structures with varying O/F. Therefore, we introduce the compression function defined here and try to capture the flow features:

$$C(\boldsymbol{x}) \equiv (\text{grad } p/p_c) \cdot (\boldsymbol{u}/|\boldsymbol{u}|)$$

This function becomes positive (negative) when the pressure increases (decreases) along a streamline. Note that this function has a dimension of per meter. Figures 11 and 12 show the compression function applied to the same computational results of Figs. 9 and 10. The schematic of the flow structure inside the CTP nozzle is presented in Fig. 13. The black part indicates the expansion region where the flow is efficiently expanded by the nozzle. The gray to white gradation, including the shock wave detected by the shock function, indicates the region where the flow is not expanded or accelerated efficiently. A strong correlation is observed between this low-expansion region and the contour of the Mach number. The concentrated and bending contour corresponds closely to the

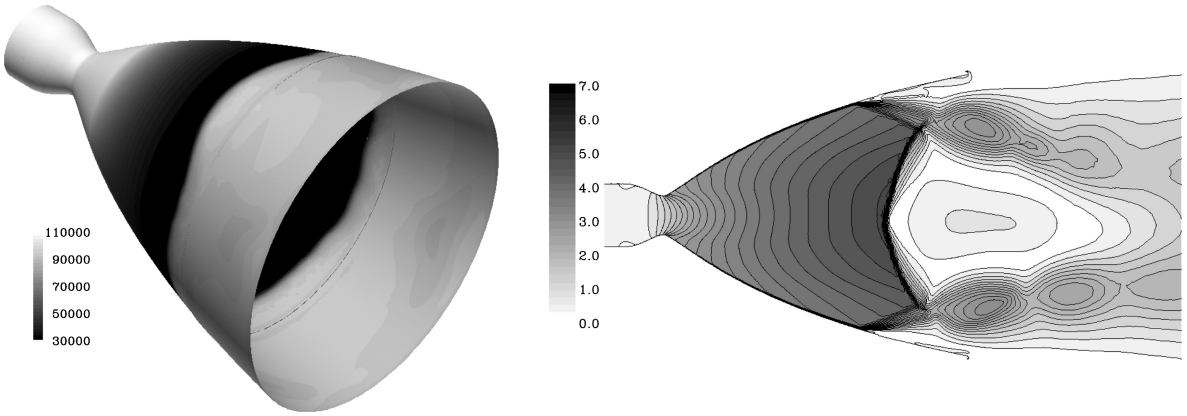

a) NPR = 49

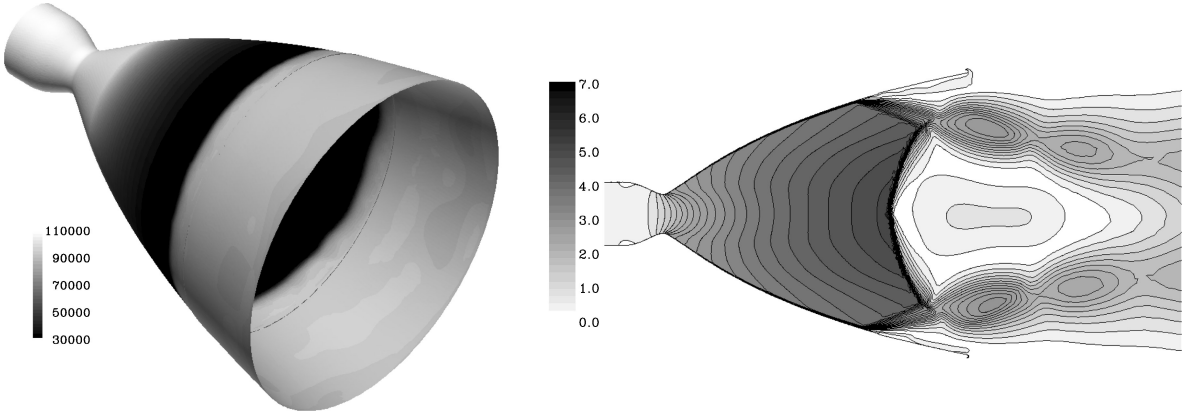

b) NPR = 50

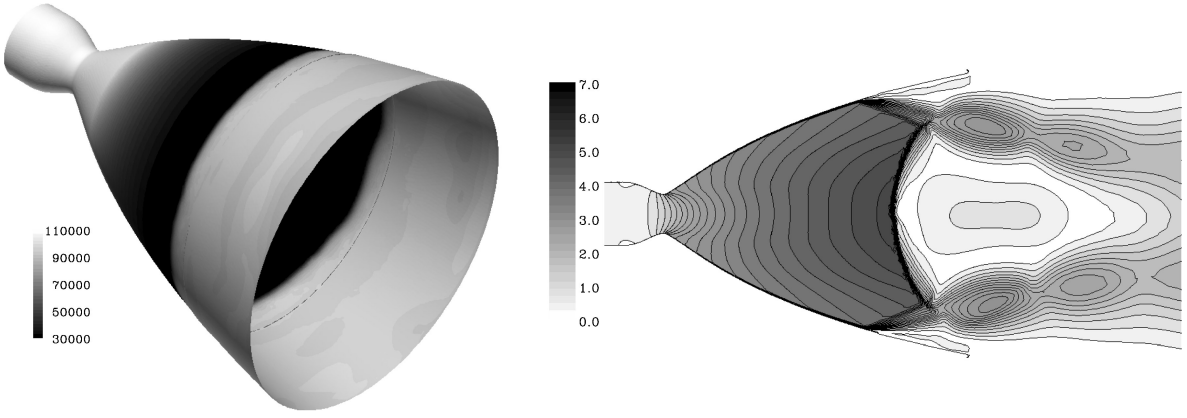

c) NPR = 51

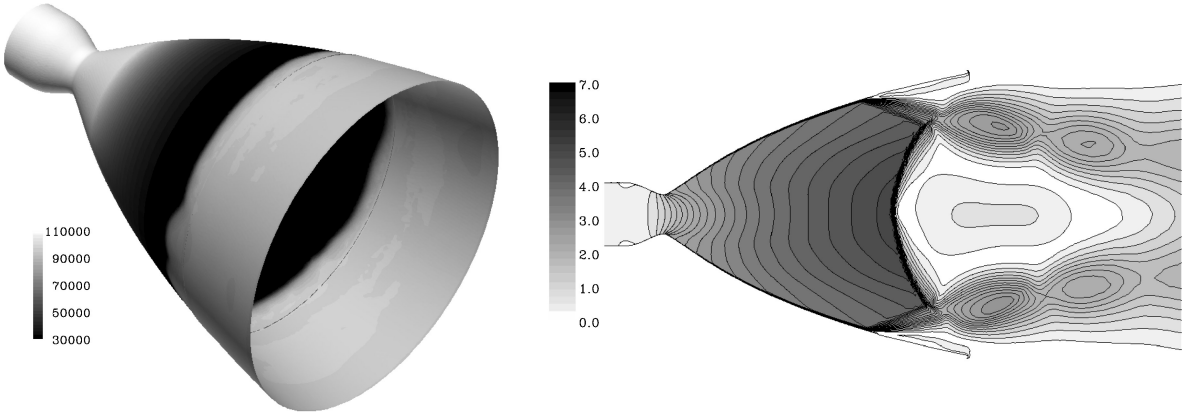

d) NPR = 52

Fig. 7 Wall pressure (pascals; left) and Mach number distribution (right), *O*/*F* = 6.

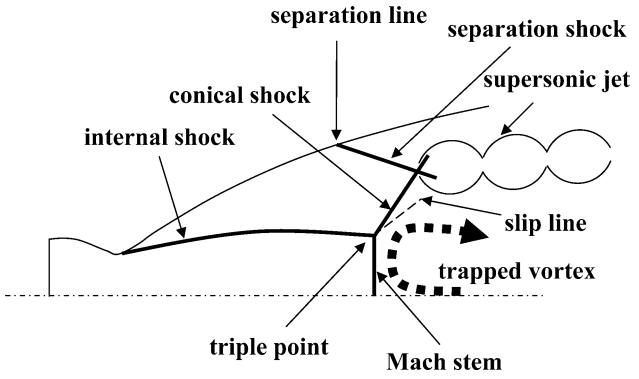

Fig. 8 Schematic of flow structure inside thrust optimized or parabolic nozzle, Vulcain or space shuttle main engine nozzle.

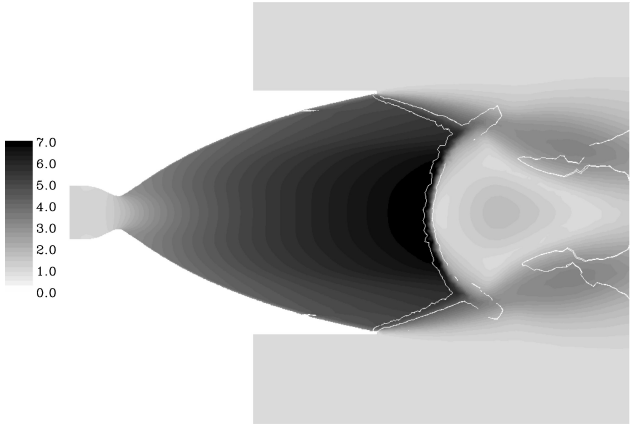

Fig. 9 Shock function (white points) and Mach number distribution, *O*/*F* = 3, full-flow condition, NPR = 124.

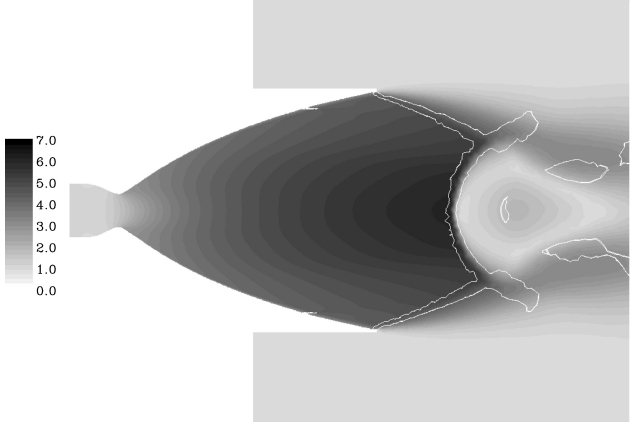

Fig. 10 Shock function (white points) and Mach number distribution, *O*/*F* = 6, full-flow condition, NPR = 124.

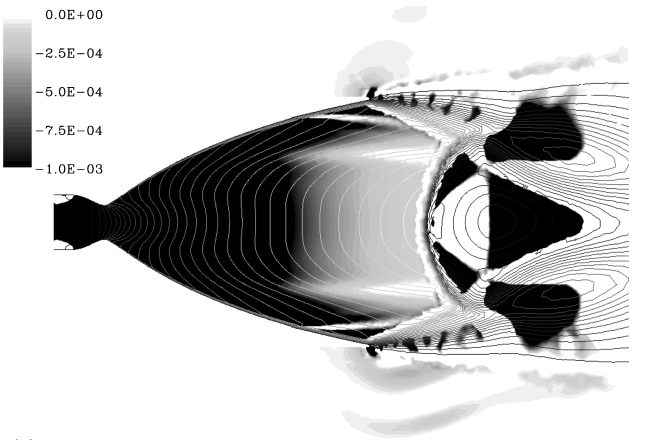

Fig. 11 Compression function (per meter) and Mach number distribution (contours), *O*/*F* = 3, full-flow condition, NPR = 124.

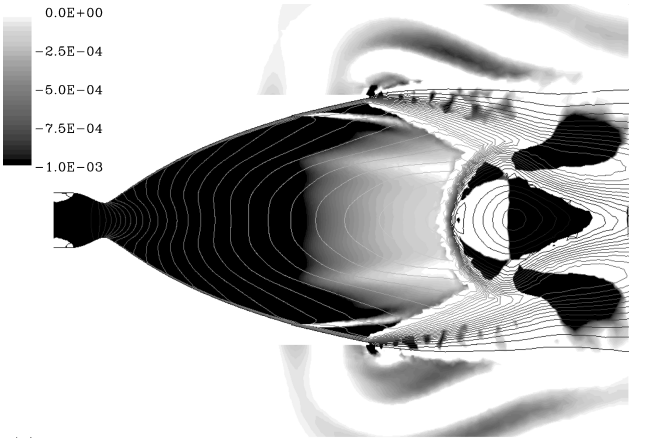

Fig. 12 Compression function (per meter) and Mach number distribution (contours), *O*/*F* = 6, full-flow condition, NPR = 124.

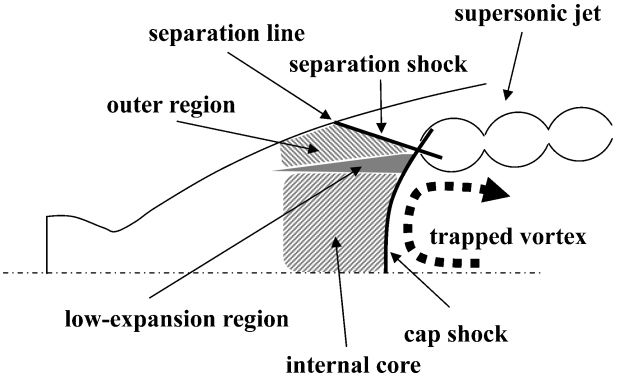

Fig. 13 Schematic of flow structure inside compressed truncated perfect nozzle, LE-7A original nozzle.

low-expansion region (thin triangular white region). By this low-expansion region, we roughly define the internal core, where the contour of the Mach number becomes nearly perpendicular to the nozzle axis, and the outer region bounded by the separation shock from the nozzle wall (Fig. 13).

If the $O/F = 3$, the internal core becomes broad radially. Therefore, the curvature of the Mach isolines is small. This results in a small curvature of the cap shock downstream. It is quite natural that the curvatures are similar because the shock wave is formed to balance the flows passing through the shock wave itself. For example, when the NPR equals 10, both the curvature of the Mach isolines and the shock downstream are convex as seen from the nozzle exit (Fig. 14). Therefore, the flow behind the shock is bent toward the symmetry axis (contrary to the flow behind a cap shock), which does not strengthen the trapped vortex observed behind a cap shock.

Another notable point is that the radial widths of the outer boundary of the low-expansion region and the end of the cap shock are nearly identical. For TO or parabolic nozzles with an internal shock, the contour of the Mach number inside the internal core region is nearly straight, generating the normal shock (Mach stem) downstream. In this case, the Mach stem and the conical shock are clearly distinguished (Fig. 8). For the CTP nozzle studied here, the low-expansion region could include a weak shock. Therefore, if we think that the low-expansion region corresponds to the internal shock inside the TO or parabolic nozzle, the flow structures look

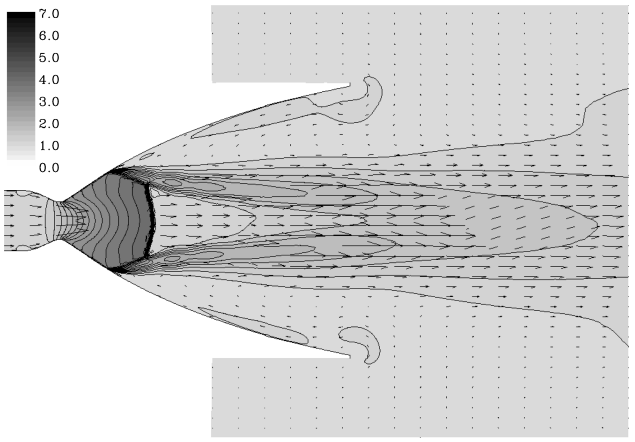

Fig. 14 Mach number and velocity vector (only subsonic part shown), *O/F* = 6, NPR = 10.

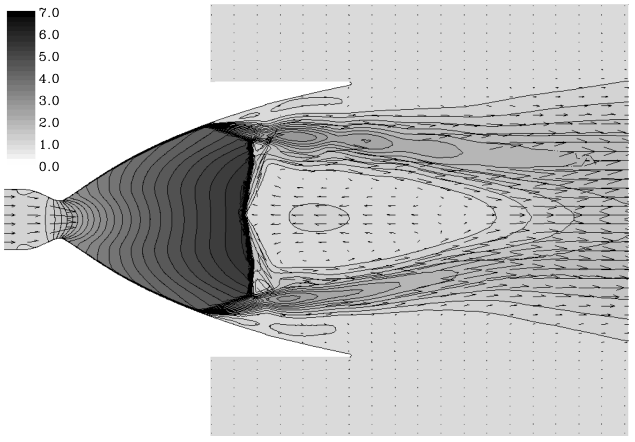

Fig. 15 Mach number and velocity vector (only subsonic part shown), *O/F* = 3, NPR = 40.

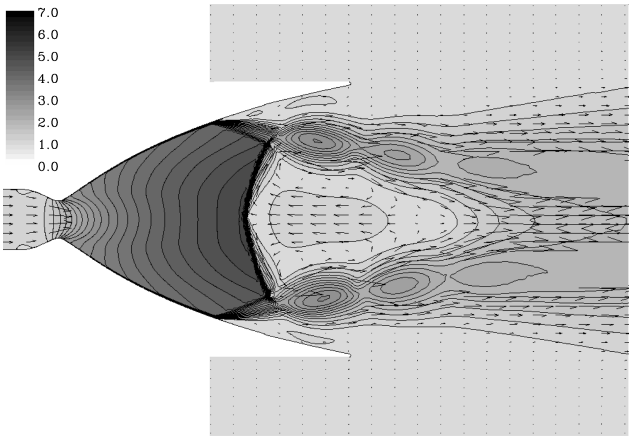

Fig. 16 Mach number and velocity vector (only subsonic part shown), *O/F* = 6, NPR = 40.

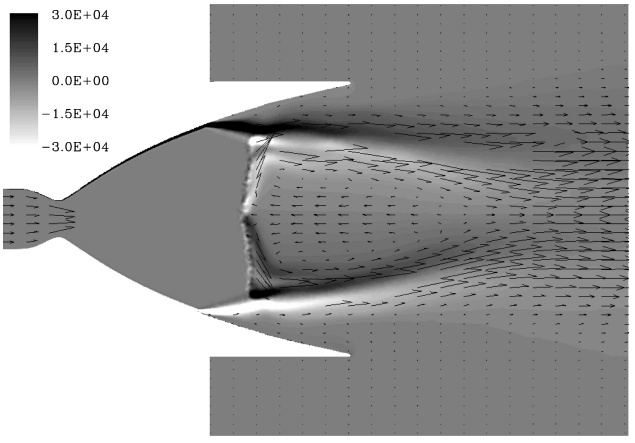

Fig. 17 *Z* component of vorticity (per second) and velocity vector (only subsonic part shown), *O/F* = 3, NPR = 40.

similar qualitatively. However, because the low-expansion region has a small effect on changing the flow structure downstream, the Mach stem and conical shock are not clearly distinguished but united to form a smooth cap shock.

Because there is no precise theory to describe the Mach reflection or the oblique shock in an axisymmetric flow configuration, it is very difficult to explain analytically the flow structure inside a nozzle. However, note that the compression function introduced here reveals a strong correlation between the outer boundary radial widths of the low-expansion region and the end of the cap shock. This function captures the mild compression flow structure inside the nozzle where an internal shock is not detected and helps in understanding the flow transition between FSS and RSS.

O/F Effect on Flow Transition

Based on the knowledge just obtained, we next consider why the transition occurs only when the mixture ratio equals three by comparing the flow structure just before the transition to RSS, NPR = 40. The causes of the flow transition in the LE-7A original nozzle are summarized as follows:

1) The first cause is the difference of the distance between the supersonic jet and the nozzle wall. Figures 15 and 16 show the Mach number distribution and velocity vector where the flow is subsonic. When $O/F = 3$, as we have shown in Figs. 11 and 12, the low-expansion region becomes broad radially. This makes the cap shock broad radially, and the supersonic jet widens downstream. Therefore, a broad circulation region (trapped vortex) is created and the supersonic jet is nearer to the wall.

2) The second cause is the difference of the trapped vortex behind the cap shock. When $O/F = 3$, the contour of the Mach number inside the internal core region is nearly straight (Fig. 15). As a result, the curvature of the cap shock, which is concave as seen from the nozzle exit, shrinks. Therefore, the radial component of the momentum (toward the nozzle wall) behind the cap shock is small (maximum value of about 60 kg/m$^2 \cdot$ s). Also, as shown in Fig. 17, the z component (perpendicular to the paper) of the vorticity behind the cap shock is small. When $O/F = 6$, the curvature of the cap shock increases compared to that when $O/F = 3$, locally generating an oblique shock (Fig. 16). It makes nearly all of the flow behind the cap shock remain supersonic, which creates the large radial component of the momentum (maximum value of about 90 kg/m$^2 \cdot$ s) and the large vorticity (higher contrast of positive and negative vorticity behind the cap shock in Fig. 18 compared to that in Fig. 17).

Figures 19 and 20 show the pressure distribution and the velocity vector just explained. When $O/F = 3$, the shock cell structure is observed. However, the series of pressure increase and decrease is weak and asymmetric. In contrast, when $O/F = 6$, the shock cell structure inside the supersonic jet is symmetric and coherent.

The trapped vortex is bounded by the supersonic jet and the first pressure rise in the wake region. When $O/F = 6$, the first pressure rise in the wake region is large (maximum value of 0.130 MPa) because the strong supersonic jet becomes narrow and interacts downstream. The large pressure difference between this rise and the region behind the cap shock generates the large backward velocity (maximum value of 590 m/s), enhancing the circulation. When $O/F = 3$, the backward velocity is low (maximum value of 450 m/s) because of the small pressure difference (maximum value of the first pressure rise of 0.113 MPa). As a result, when $O/F = 6$, there is a strong local trapped vortex downstream of the cap shock.

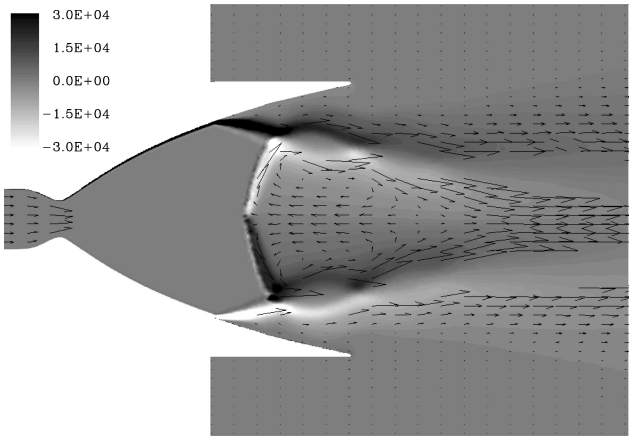

Fig. 18 *Z* component of vorticity (per second) and velocity vector (only subsonic part shown), *O/F* = 6, NPR = 40.

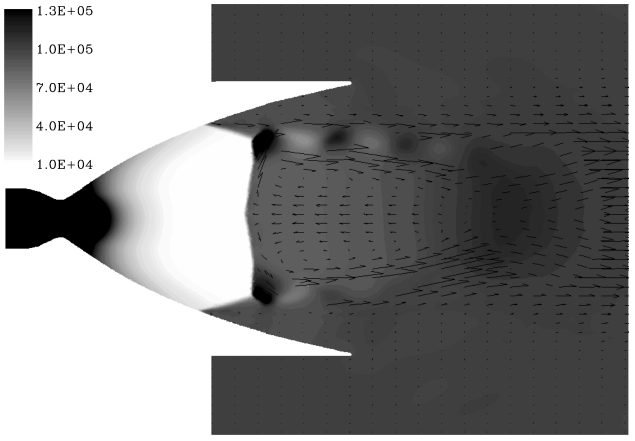

Fig. 19 Pressure (pascals) and velocity vector (only subsonic part shown), *O/F* = 3, NPR = 40.

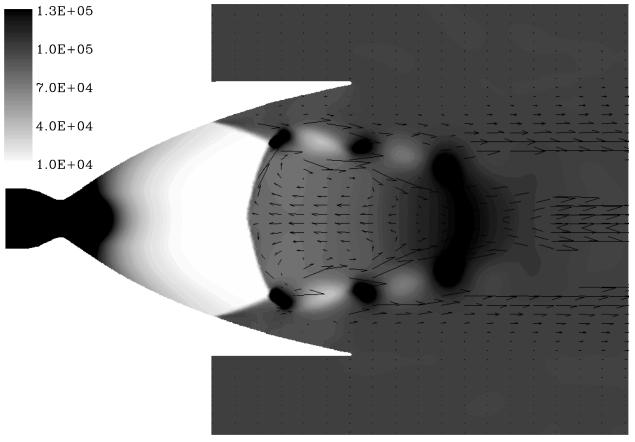

Fig. 20 Pressure (pascals) and velocity vector (only subsonic part shown), *O/F* = 6, NPR = 40.

The supersonic jet, which includes a series of shock waves and expansion waves, inherently has an unsteady nature and is the most essential origin of the instability of the whole flow structure. The fluctuation of the pressures in the separated region is another source of the disturbance of the separation line because the location of the line depends on the NPR. The whole flow structure including the shock structures and trapped vortex is always exposed to the disturbances mentioned earlier. As we have explained, once the supersonic jet approaches the nozzle wall enough to decrease the wall pressure, the supersonic jet suddenly reattaches to the wall. Therefore, when $O/F = 3$, because the supersonic jet becomes broad radially and the weak circulation is unstable against the disturbances, the flow is likely to become RSS. When $O/F = 6$, the flow structure is relatively coherent and remains FSS. In the LE-7A engine, the O/F fluctuates sharply at the transient. Therefore, the supersonic jet is repeatedly widened and narrowed, increasing the instability of the shocks' flow structure and the trapped vortex behind them. In addition to detecting the obvious flow structures, such as a cap shock and an internal shock, we found that understanding the fine structure of the flow is the key in determining whether the flow becomes RSS or FSS in the CTP nozzle.

Here, we will briefly mention the RSS flow at the shutdown transient. Generally speaking, the RSS flow is more likely to be generated by a shutdown transient than a startup transient. When the NPR is decreased from the full-flow condition (FSS flow), the separation line and separation shock move upstream slowly due to the viscous effect. In other words, the hysteresis of the location of the separation line is observed. At the same NPR, the separation line of the shutdown transient is located further downstream than that of the startup. The hysteresis of the location of the cap shock is smaller than that of the separation line. As a result, the axial positions of the separation line and cap shock become closer or reversed at the shutdown transient, and the structure approaches that of an RSS flow.

Summary

The transition of the flow structure from FSS to RSS inside a CTP nozzle was numerically reproduced and explained. The mixture ratio is the key to determining flow structure. A simple method using the compression function is proposed to capture the flow structure and understand the transition; the method is especially valid for the flow without an internal shock that is easily detected by the shock function. This method can be applied to the result of steady full-flow calculation to investigate the low-expansion region that affects the important flow structure downstream, such as in a supersonic jet and a trapped vortex. Because there is no internal shock detected inside the CTP nozzle studied here, the transition to RSS is less likely to occur than in the TO and parabolic nozzles. However, with an off-design mixture ratio, the contour of the Mach number connecting the internal core and outer region bends more than that for the design mixture ratio, widening the internal core region where the flow is accelerated and expanded. Thus, the flow structure becomes closer to that inside TO or parabolic nozzles. To avoid FSS–RSS transition so that the side load in startup and shutdown transients is within a permissible level, a transient simulation under an off-design mixture ratio is recommended.

References

[1]Zucrow, M. J., and Hoffman, J. D., *Gas Dynamics*, Vol. 2, Wiley, New York, 1977, pp. 160–164.

[2]Rao, G. V. R., "Exhaust Nozzle Contour for Optimum Thrust," *Jet Propulsion*, Vol. 28, No. 6, 1958, pp. 377–382.

[3]Hoffman, J. D., "Design of Compressed Truncated Perfect Nozzles," *Journal of Propulsion*, Vol. 3, No. 2, 1987, pp. 150–156.

[4]Nave, L. H., and Coffey, G. A., "Sea Level Side Loads in High-Area-Ratio Rocket Engines," AIAA Paper 73-1284, Nov. 1973.

[5]Frey, M., and Hagemann, G., "Restricted Shock Separation in Rocket Nozzles," *Journal of Propulsion and Power*, Vol. 16, No. 3, 2000, pp. 478–484.

[6]Hagemann, G., Frey, M., and Koschel, W., "Appearance of Restricted Shock Separation in Rocket Nozzles," *Journal of Propulsion and Power*, Vol. 18, No. 3, 2002, pp. 577–584.

[7]Östlund, J., Damgaard, T., and Frey, M., "Side-Load Phenomena in Highly Overexpanded Rocket Nozzles," *Journal of Propulsion and Power*, Vol. 20, No. 4, 2004, pp. 695–704.

[8]Onofri, M., and Nasuti, F., "The Physical Origins of Side Loads in Rocket Nozzles," AIAA Paper 99-2587, June 1999.

[9]Deck, S., and Guillen, P., "Numerical Simulations of Side Loads in an Ideal Truncated Nozzle," *Journal of Propulsion and Power*, Vol. 18, No. 2, 2002, pp. 261–269.

[10]Verma, S. B., "Study of Flow Separation in Truncated Ideal Contour Nozzle," *Journal of Propulsion and Power*, Vol. 18, No. 5, 2002, pp. 1112–1121.

[11]Gross, A., Haidn, O., Stark, R., Zeiss, W., Weber, C., and Weiland, C., "Experimental and Numerical Investigation of Heat Loads in Separated Nozzle Flow," AIAA Paper 2001-3682, July 2001.

[12]Gross, A., and Weiland, C., "Numerical Simulation of Separated Cold Gas Nozzle Flows," *Journal of Propulsion and Power*, Vol. 20, No. 3, 2004, pp. 509–519.

[13]Deck, S., and Nguyen, A. T., "Unsteady Side Loads in a Thrust-Optimized Contour Nozzle at Hysteresis Resime," *AIAA Journal*, Vol. 42, No. 9, 2004, pp. 1878–1888.

[14]Wang, T.-S., "Transient Three-Dimensional Analysis of Side Load in Liquid Rocket Engine Nozzles," AIAA Paper 2004-3681, July 2004.

[15]Watanabe, Y., and Tsuboi, M., "LE-7A Engine Nozzle Problems During Transient Operations," AIAA Paper 2002-3841, July 2002.

[16]Tomita, T., Sakamoto, H., Takahashi, M., Sasaki, M., Tamura, T., and Tsuboi, M., "Sub-Scale Nozzle Combustion Tests of the LE-7A Engine for Clarification of Large Side-Loads (I): Formation of RSS Structure Due to Combustion Condition," AIAA Paper 2002-3842, July 2002.

[17]Tomita, T., Sakamoto, H., Onodera, T., Sasaki, M., Takahashi, M., Tamura, H., and Watanabe, Y., "Experimental Evaluation of Side-Load Characteristics on TP, CTP and TO Nozzles," AIAA Paper 2004-3678, July 2004.

[18]Yonezawa, K., Yokota, K., Tsujimoto, Y., Sakazume, N., and Watanabe, Y., "Three-Dimensional Unsteady Flow Simulation of Compressed Truncated Perfect Nozzles," AIAA Paper 2002-3991, July 2002.

[19]Takahashi, M., Ueda, S., Tomita, T., Takahashi, M., Tamura, H., and Aoki, K., "Transient Flow Simulation of a Compressed Truncated Perfect Nozzle," AIAA Paper 2001-3681, July 2001.

[20]Nasuti, F., and Onofri, M., "Viscous and Inviscid Vortex Generation During Startup of Rocket Nozzles," *AIAA Journal*, Vol. 36, No. 5, 1998, pp. 809–815.

[21]Chen, C. L., Chakravarthy, S. R., and Hung, C. M., "Numerical Investigation of Separated Nozzle Flows," *AIAA Journal*, Vol. 32, No. 9, 1994, pp. 1836–1843.

[22]Kodera, M., Sunami, T., and Nakahashi, K., "Numerical Analysis of SCRAMJET Combusting Flows by Unstructured Hybrid Grid Method," AIAA Paper 2000-0886, Jan. 2000.

[23]Goldberg, U. C., and Ramakrishnan, S. V., "A Pointwise Version of Baldein–Barth Turbulence Model," *Computational Fluid Dynamics*, Vol. 1, No. 4, 1993, pp. 321–338.

[24]Venkatakrishnan, V., "On the Accuracy of Limiters and Convergence to Steady State Solutions," AIAA Paper 93-0880, Jan. 1993.

[25]Kano, S., Yamamoto, S., and Daiguji, H., "An Efficient CFD Approach for Simulating Unsteady Hypersonic Shock–Shock Interference Flows," *Computers and Fluids*, Vol. 27, Nos. 5–6, 1998, pp. 571–580.

[26]Lovely, D., and Haimes, R., "Shock Detection from Computational Fluid Dynamics Results," AIAA Paper 99-3285, July 1999.

C. Kaplan
Associate Editor